

# Comparative Analysis of Dual Stator Machines



C.C. Awah



Department of Electrical and Electronic Engineering, Michael Okpara University of Agriculture, Umudike

**ABSTRACT:** Electromagnetic performance of three different types of double stator permanent magnet machine is analyzed and compared in this study. The analyzed machines in this study are Machine 1, Machine 2 and Machine 3. These machines are designated as: M 1, M 2 and M 3, respectively. The studies are implemented using two-dimensional and three-dimensional finite element analysis (2D-FEA and 3D-FEA) methods. The predicted performance indices are: total harmonic distortion of the voltage, torque ripple, cogging torque, winding inductances, output torque and unbalanced magnetic force (UMF). The studies show that the investigated machine types have negligible reluctance torque and thus, similar axes inductance values. Therefore, the machines' bulk torque components are contributed mainly by the magnets while the armature excitation sources yield lesser torque components. Amongst the compared machines, M 3 type has an outstanding performance in almost all the performance metrics, compared to M 2 and M 1 types. Nevertheless, M 1 machine type has some good attributes, particularly, with respect to its high output torque per applied magnet volume, in addition to its widest operating speed range ability. Low-speed high-torque applications are most suitable for the investigated machines in practice.

**KEYWORDS:** Field vectors, inductances, torque, torque ripple and magnetic force

[Received July 2, 2023; Revised Oct. 31, 2023; Accepted Nov. 15, 2023]

Print ISSN: 0189-9546 | Online ISSN: 2437-2110

## I. INTRODUCTION

Higher output torque and power densities as well as enhanced efficiency are some of the desirable features of permanent magnet (PM) machines over the PM-free ones. However, these advantages often come with high-cost penalty, especially, when high-energy density rare-earth magnetic materials are deployed. More so, it is established in Raza *et al.*, (2017) and Asgaria *et al.*, (2022) that improved machine performances could be obtained from double stator electric machines compared to their single stator equivalents. Hence, three different kinds of double stator permanent magnet (DSPM) machines are developed and compared in this study, for improved electromagnetic performances.

Although, DSPM machines usually exhibit enhanced output performances than their single stator counterparts; it is proved in Zhao *et al.*, (2022) that DSPM machine would always have higher split ratio and would yield inferior output performance if the shaft size is excessively enlarged. Hence, the improved performance of a given DSPM machine is only sustainable at an optimal shaft size. Also, a dual rotor electric generator would have relatively higher voltage and power density than its dual stator equivalent; albeit, with increased mechanical and technical complications, as reported in Ullah *et al.*, (2022). However, it is noted in the work of Xie *et al.*, (2022) that larger torque density and improved control flexibility would be realized from dual stator electric motor.

A high torque dual stator PM machine having consequent-pole structure is proposed in Baloch *et al.*, (2018), but it could be inferred that the acclaimed consequent-pole machine may suffer from magnet instability. The instability flaw is as a result of the adopted surface-mounted-magnet topology. The dual stator consequent-pole machine also has potential eddy current loss issues, due to the adopted rotor-PM style of the machine. The increased eddy current loss may eventually affect the efficiency of the machine, apart from its complicated mechanical structure. Similarly, a DSPM machine of different structural topology is recommended in Kwon *et al.*'s work (2018); however, the recommended machine would attract high joule loss coupled with increased cost implication, due to its deployed distributed winding configuration. Additionally, it would have reduced overall efficiency compared with an equivalent machine that is equipped with concentrated winding. Note that the compared machines in this current study have concentrated windings and would exhibit larger operating speed range than that recommended in the study conducted by Kwon *et al.*, (2018).

Furthermore, a DSPM machine having flux-reversal skill is analyzed in by Yu *et al.*, (2019). In general, flux-reversal machines are usually associated with high flux leakages and low power factor feature; though, the analyzed flux-reversal DSPM machine seems to have an improved reliability compared to a given traditional permanent magnet machine. Moreover, an analytical investigation of segmented dual stator

PM machine presented in Vahaj *et al.*, (2019) shows that magnetization direction of permanent magnets (PMs) is paramount in determining the overall electromagnetic output of the machine. Halbach magnetization arrangement is recommended to yield the best output performance; though, the analysis may not be completely accurate owing to the series of assumptions that are intrinsically linked to finite element analytical studies.

Also, the report presented by Zhao *et al.*, (2021) revealed that, by optimizing the geometric dimensions of a given electric machine, then, its output performance such as torque density and fault-tolerance could be greatly enhanced; nevertheless, the presented machine in Zhao *et al.*, (2021) has an overwhelming complex architecture.

In this present investigation, three different machine topologies of double stator permanent magnet machines are developed and its electromagnetic performances compared comprehensively; for possible implementation in direct-drive low-speed high-torque in-wheel vehicle and traction applications.

## II. MATERIALS AND METHOD

Two- and three-dimensional (2D- and 3D-) finite element analyses (FEA) are deployed in predictions of the performance indices in this study, using ANSYS-MAXWELL Version 16.0 software. The time-stepping magnetic transient solution method is employed in the analysis. It is worth noting that the rotor of developed machines is free of both windings and permanent magnets (PMs); hence, low eddy current loss is achievable in such electric machines. More so, simple cooling arrangement such as natural air cooling through the perforated casing or use of fans is easily applied, since the armature windings and the PMs are housed in the stator. The investigated machines are equipped with rare-earth magnets; specifically, the Neodymium-Iron-Boron (NdFeB) of N38SH grade, while the stator and rotor cores are made of steel material; the implemented magnetic coercivity and remanence is -909456.82 A/m and 1.2 Tesla, respectively. Meanwhile, Maxwell Stress Tensor method is implemented in the torque generation in addition to the applied tiny discretized mesh elements; especially, around the air-gap, for improved output torque. Note also that the investigated machines have three-phase windings which are excited with sinusoidal alternating current (AC). The excited phase currents have same phase angle with the induced-phase electromotive force (EMF), for effective torque production. The investigated machine models and their respective 3D-FEA magnetic field vectors are shown in Figure 1. The estimated torque ripple ( $T_{rip}$ ) and voltage total harmonic distortion ( $THD_v$ ) is calculated in Eqns. (1) and (2), respectively. The rated speed ( $\omega_m$ ) and current ( $I_{max}$ ) of the investigated machines is 400 rpm and 15 A, respectively. Moreover, the analyses are simulated at ambient temperature of 20°C. Note that the PMs are magnetized in circumferential direction, in such a manner that the closest magnets would possess opposite magnetization polarity or sign. Note also that the machine's outer radius, air-gap length and number of turns/phase are: 45 mm, 0.5 mm and 72, respectively. The compared machines are Machine 1, Machine 2 and Machine 3.

These machines are designated as: M 1, M 2 and M 3 machine types, respectively.

$$T_{rip} = \frac{\text{Maximum torque} - \text{Minimum torque}}{\text{Average torque}} \times 100\% \quad (1)$$

$$THD_v = \frac{(\sum_{n=2}^{\infty} E_n^2)^{\frac{1}{2}}}{E_1} \times 100 \quad (2)$$

where  $E_1$  is the fundamental voltage harmonic content and  $E_n$  is the  $n^{\text{th}}$  voltage harmonic order. Eqns. (3) and (4) are employed in estimating the winding inductances in the different rotor/machine axes.

$$L_d = \frac{\varphi_d - \varphi_{o.c}}{i_d} \quad (3)$$

$$L_q = \frac{\varphi_q - \varphi_{o.c}}{i_q} \quad (4)$$

where  $L_d$ ,  $L_q$ ,  $i_d$ ,  $i_q$  are the direct and quadrature axes inductances and currents, respectively,  $\varphi_d$  and  $\varphi_q$  are the direct and quadrature axes flux linkages at the rated current conditions,  $\varphi_{o.c}$  is the open-circuit flux linkage.

Furthermore, the torque-speed envelopes are calculated by using the maximum torque per ampere (MTPA) control strategy, which is implemented in the constant torque region where the direct axis current is set to zero i.e.,  $i_d = 0$  with a maximum quadrature axis current, i.e.  $I_{max} = i_q$ . Similarly, the flux-weakening control technique is employed in the constant power region by injecting negative direct-axis current, i.e.  $-I_{max} = i_d$ , in order to weaken the flux in this area while increasing the machine's speed for an extended range, at fixed voltage amplitude. The constrained voltage value in the torque-speed envelope is such that the applied voltage is restricted to maximum voltage ( $V_{max}$ ) of 36 V.

Moreover, the magnetic field lines and flux density contours of the compared machines under open-circuit condition are depicted in Figure 2. It is obvious that the regions having closer proximity to the air-gap (the rotor and stator core tips) experience higher electric loading effect than the other areas of the machine, owing to the large amount of magnetic flux densities on these sections of the machine during the energy conversion activities. This overload trend which tends to saturate the teeth tips is quite common in flux-switching permanent magnet machines (Cao *et al.*, 2012), a family of machines to which the analysed machines in this present study also belong to. More so, the least amount of flux linking the stator and rotor sections via the air gap is obtainable in M 2 machine type, as shown in Figure 2(b) and Table 1; though, there are slight flux leakages in all the compared machines. Eqns. (5) and (6) are adopted in predicting the rotor unbalanced magnetic force (UMF) in the horizontal and vertical axes of the machine, respectively.

$$F_x = \frac{Lr_g}{2\mu_0} \int_0^{2\pi} [(B_\alpha^2 - B_r^2)\cos\alpha + 2B_r B_\alpha \sin\alpha] \Delta\alpha \quad (5)$$

$$F_y = \frac{Lr_g}{2\mu_0} \int_0^{2\pi} [(B_\alpha^2 - B_r^2)\sin\alpha - 2B_r B_\alpha \cos\alpha] \Delta\alpha \quad (6)$$

The consequential force magnitude on the rotor ( $F$ ) is given by  $F = \sqrt{F_x^2 + F_y^2}$ .

where  $r_g$  is the radius of the air gap,  $\mu_0$  is air permeability,  $L$  is the effective stack length,  $B_\alpha$  and  $B_r$  is the circumferential and radial elements of the air gap flux density  $F_x$  and  $F_y$  are the respective horizontal and vertical force components (Chen and Zhu, 2010).

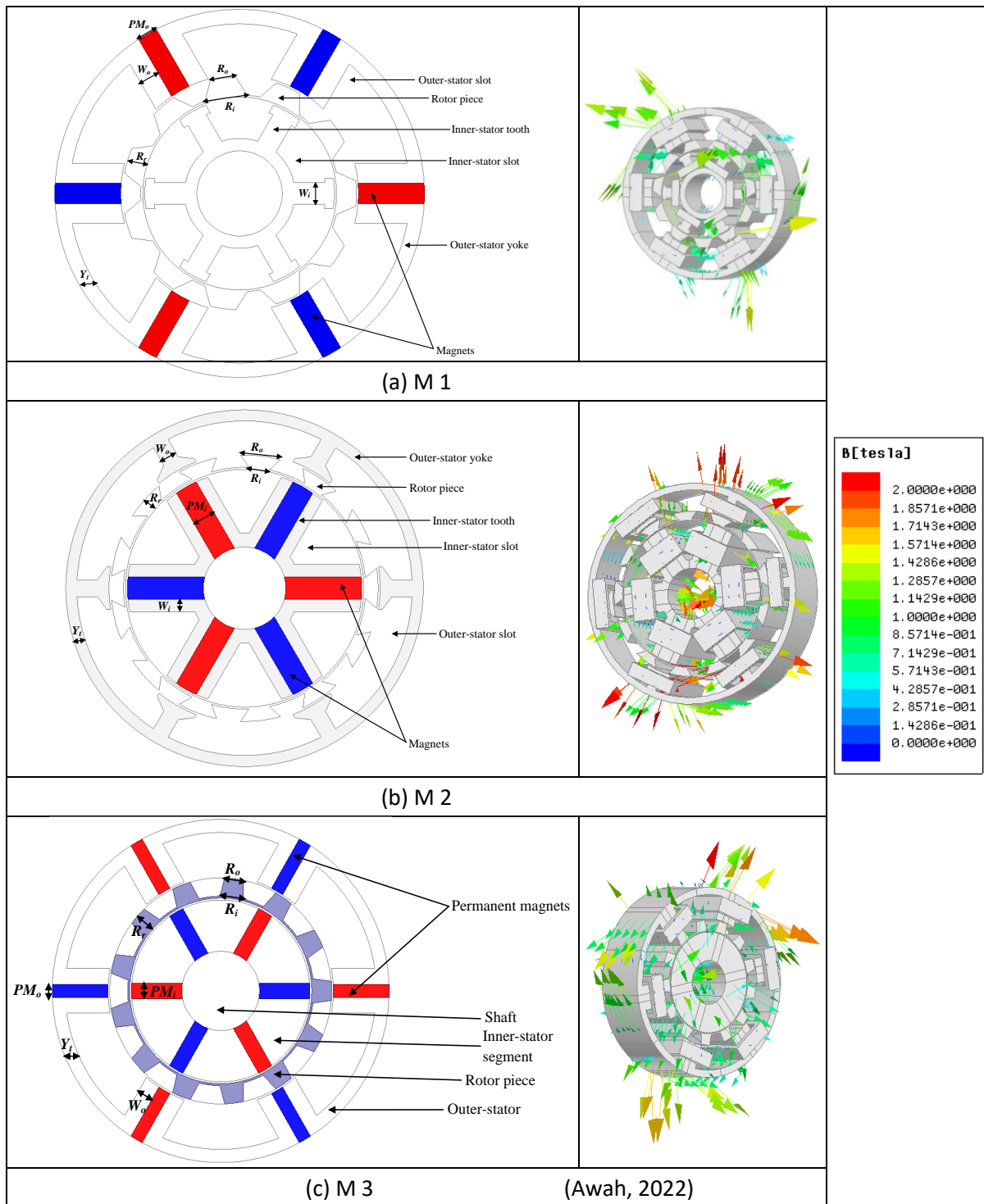


Figure 1. Schematic of the analysed machines and its magnetic field vectors.

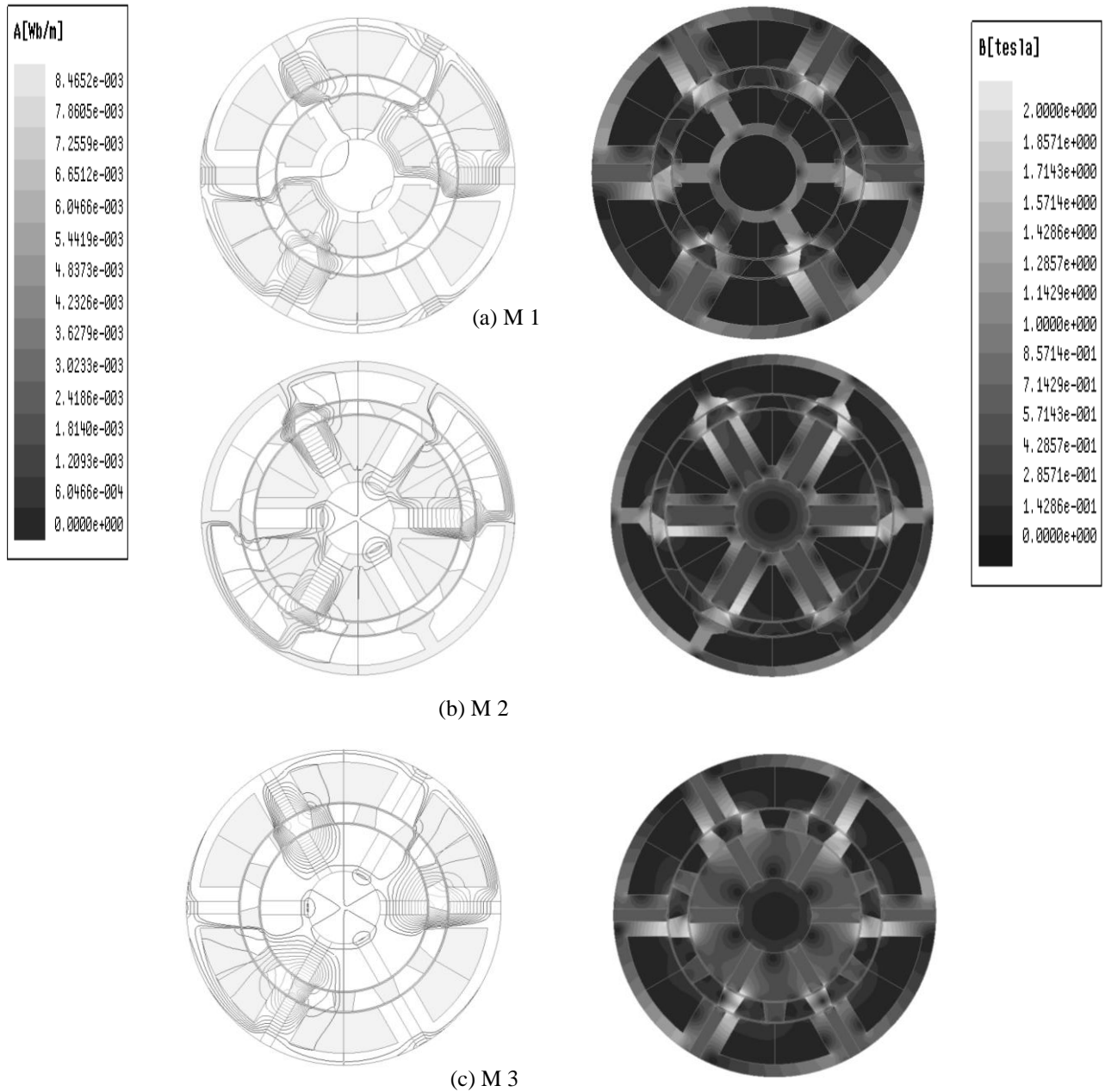


Figure 2. Flux lines and flux density distributions of the analysed machines at 15 A, 2D-FEA.

### III. RESULTS AND DISCUSSION

#### A. Torque and Voltage Characteristics

The air gap flux density waveforms of the compared machines are shown in Figure 3(a).

It is clear that the waveforms are not completely symmetrical over the simulated rotor positions and hence, over the simulation time. This is likely due to undesirable harmonic effects around the air gap region. More so, the dominant harmonic orders are mainly the odd-numbered ones i.e. 1st, 3rd, 5th, 7th etc., as recorded in Figure 3(b). The cogging torque cycles and its resulting harmonic orders are displayed

in Figure 4. It is shown in Figure 4(b) that the most prominent harmonic order of the analyzed machines is the sixth ( $6^{\text{th}}$ ), which corresponds to the number of no-load torque cycles in one electric revolution of a given flux switching machine, i.e. six cycles per electrical period in the present cases. It should be noted that the cogging torque waveform of M 2 is asymmetric over the rotor positions, and it has the largest amount of cogging torque value compared to the other machines; this is possibly due to its enormous harmonic influence, this would eventually give rise to high amount of torque ripple in the device, as recorded in Table 1. Since large amount of this undesirable torque component could lead to

mechanical instability in the system (Jo *et al.*, 2019), appropriate skewing technique could be employed in order to mitigate or reduce the amount of cogging torque in a machine; though, with some reductions in its output torque as a price.

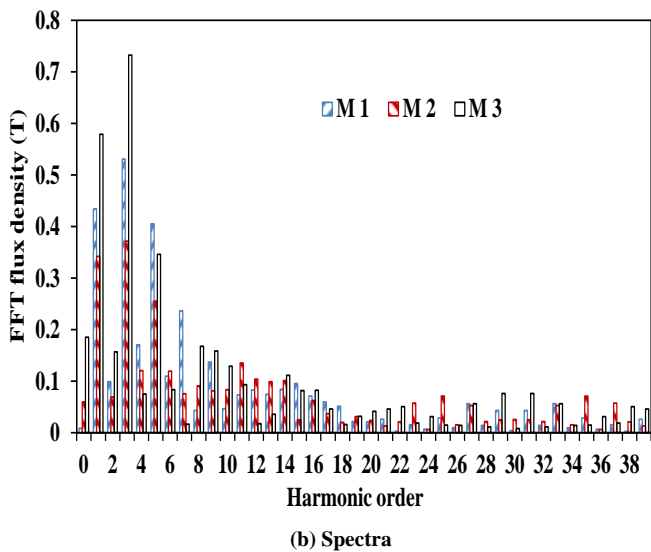
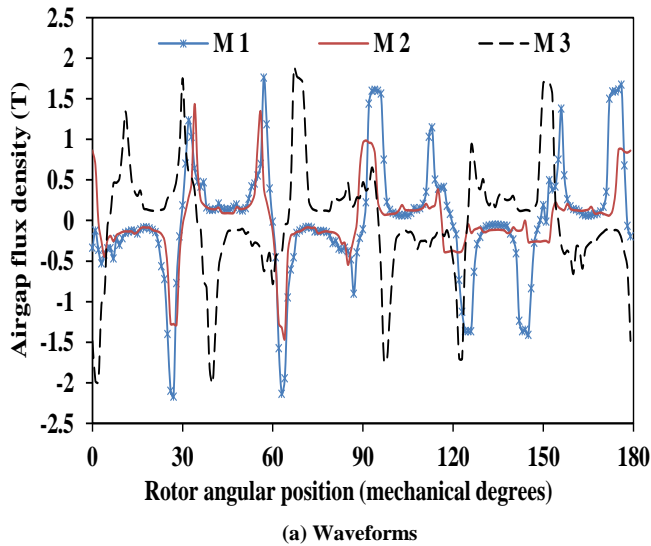


Figure 3. The airgap flux density, 2D-FEA.

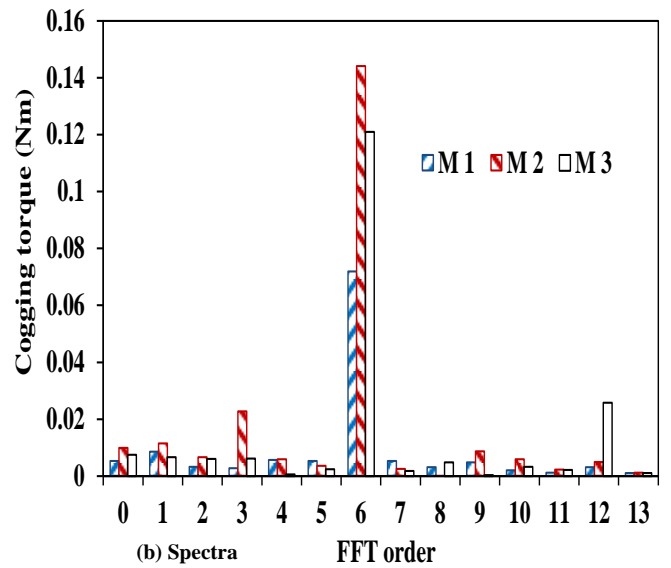
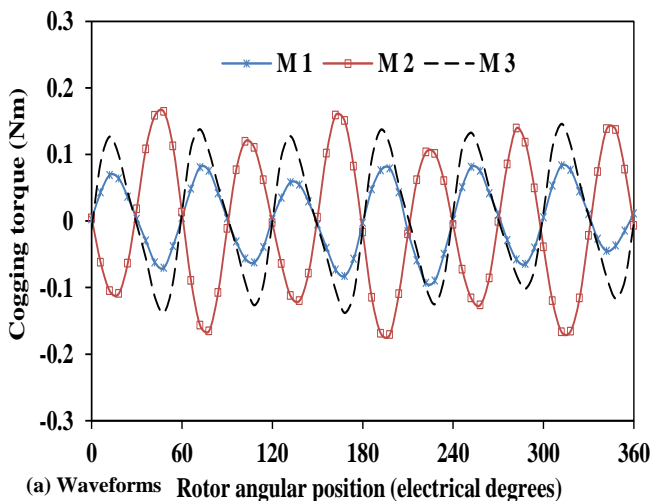
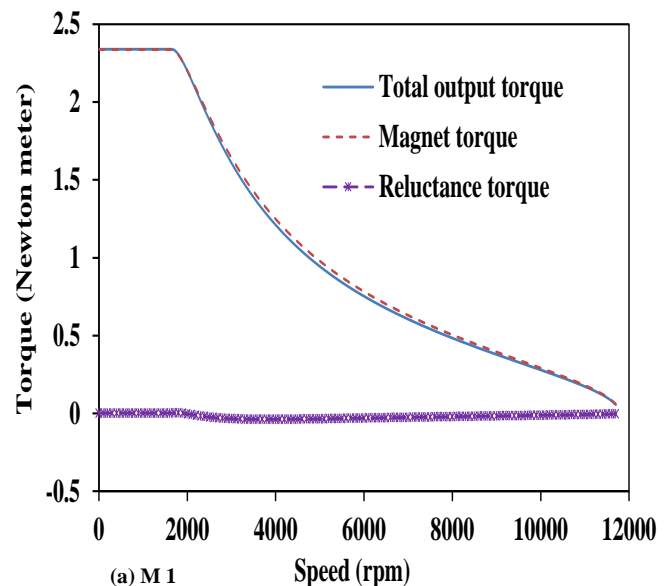


Figure 4. The cogging torque, 2D-FEA.

Figure 5 shows the torque-speed curves of the compared machines. Clearly, it is shown that M 3 has the largest output torque and all the analyzed machines have negligible reluctance torque. More so, it is evident that in all cases, the torque component due to the magnets is significantly large, since it is at par with the total output torque, as observed from Figure 5. Note that M 1 has the widest operating speed range, which would be good for vehicle driving cycle. However, the speed range of any given electrical machine may be considerably extended by deploying a hybridized excitation winding topology, to enable both flux-enhancement and flux-weakening modes by regulating the direct current (DC) source of the hybrid system, as demonstrated in Yu *et al.*, (2020). Nevertheless, this method would create additional control issues or complexity and hence, increased cost with regard to implementing suitable power electronic devices and techniques.



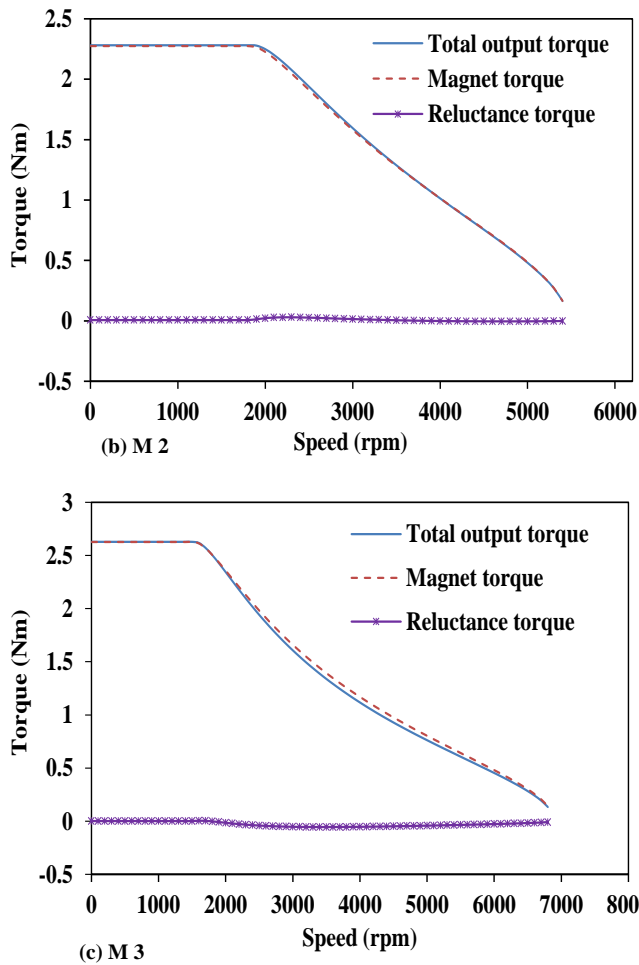


Figure 5. The torque-speed envelopes at rated current, 2D-FEA.

The resultant torque in the analyzed machines is directly proportional to its phase EMF and would depend on the interactions between the phase induced voltages or EMFs and currents. The torque outcome is evident in the results of Figure 5 and Table 1, where M 3 takes the lead in the amount of output torque, as a direct consequence of its high electromotive force magnitude presented in Figure 6(b); though, the phase flux-linkage of M 1 seems to be the largest owing to its high flux per pole aptitude, since it is of a lesser number of rotor poles. The high flux per pole attribute of M 1 is particularly valid before the saturation or overload period, and can be extended to any given electric machine. M 2 is the weakest amongst the compared machine types, in terms of resultant fast Fourier transform (FFT) flux linkage and EMF values and subsequently, with regard to the resulting electromagnetic torque.

Since, M 3 machine configuration has the lowest total harmonic distortion (THD) under no-load condition, as established in Table 1 with a value of 1.9363 % and Figure 7(c) i.e. at origin; it is indicative that M 3 would have the most sinusoidal voltage waveform and thus, would emerge as the most promising candidate for electric machine control purposes, amongst the compared machines. Also, electric machines having low value of THD would correspondingly yield a low PM eddy current loss magnitude, as proved in

Hwang *et al.*, (2014) and reconfirmed in Table 1. More so, M 2 exhibits the highest value of torque ripple at rated current setting, this trend is in consonant with its largest cogging torque magnitude, as depicted in Figure 7(a). The predicted 3D-FEA torque ripple estimates of the investigated machines are compared in Figure 7(b).

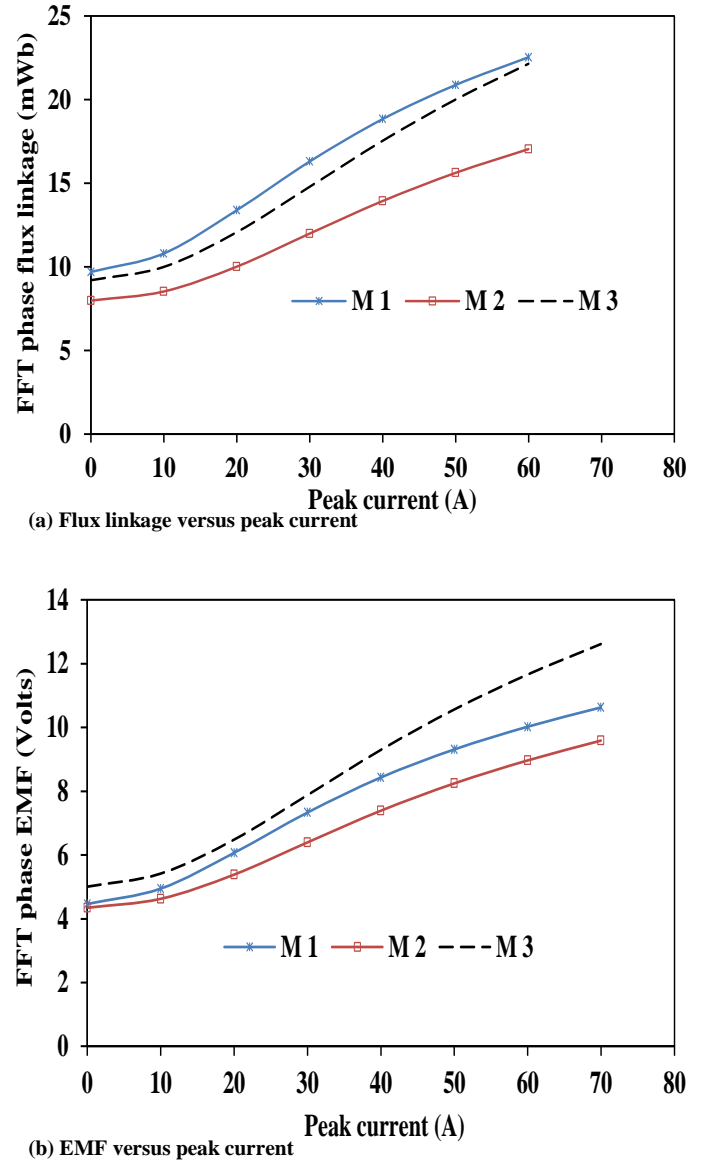


Figure 6. The phase flux linkage and EMF with current at 400 rpm, 2D-FEA.

When measured on the same scale with respect to the amount of torque produced per volume of PM material utilized; then, output performance of M 1 would overshadow that of the other compared machines, as shown in Figure 8. Invariably, considering the high price of PM materials, it would be more economical to adopt M 1, if cost is given a top priority, especially for large scale production. However, a compromise is usually made between cost-effectiveness and reliability or and efficiency, and this would be determined by the required machine application.

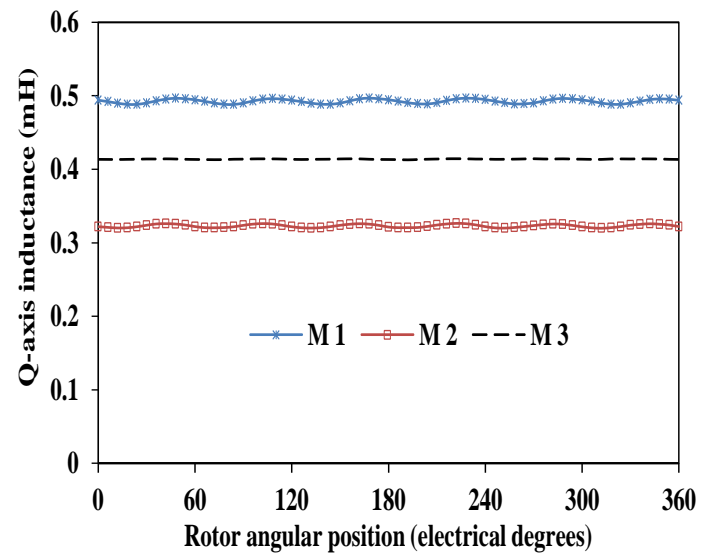
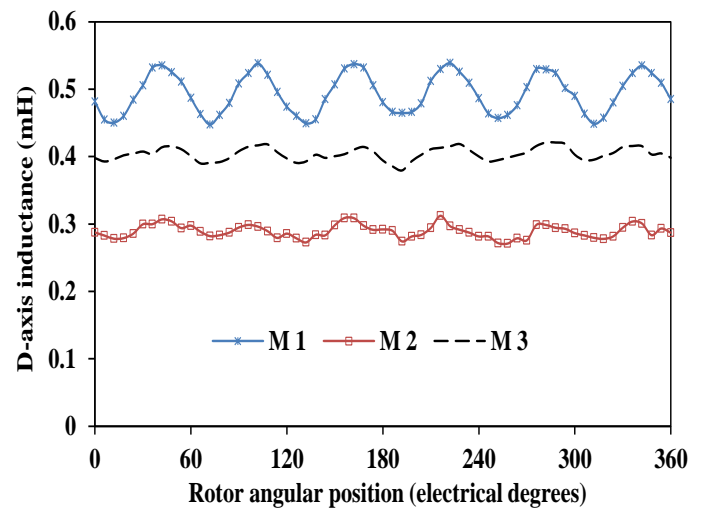
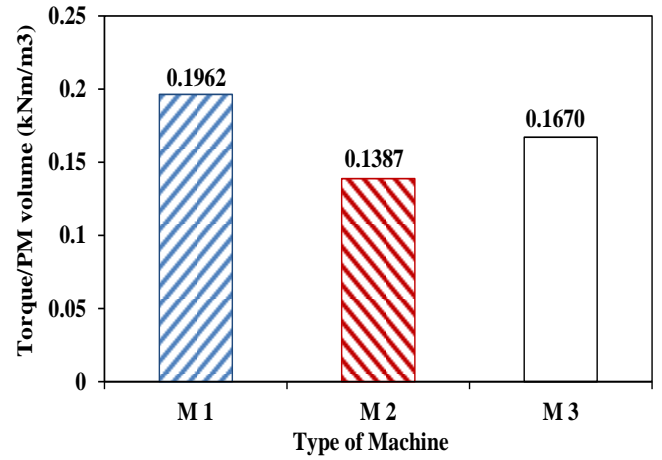
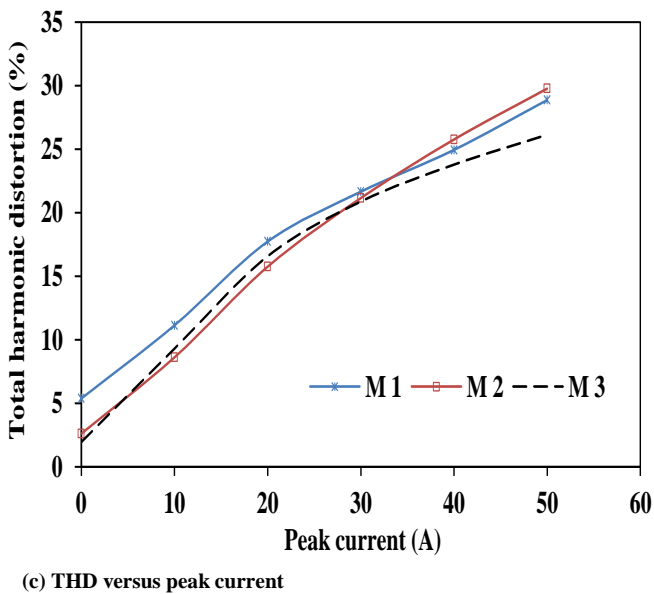
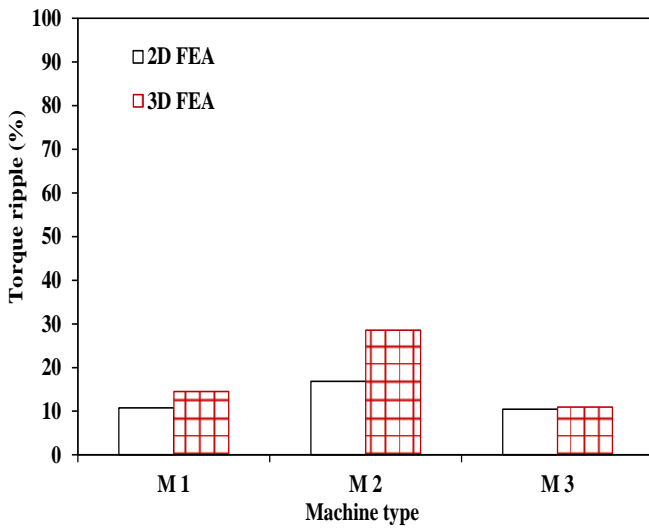
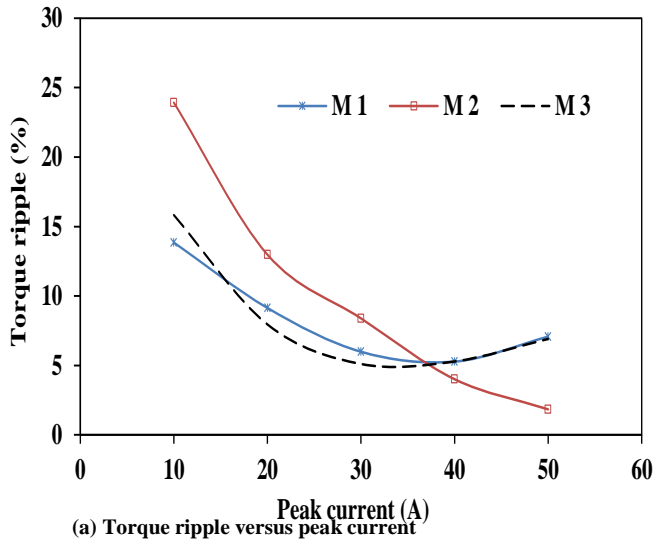


Figure 9. The winding inductances, 2D-FEA.

Figure 7. The torque ripple and THD comparisons.

**Table 1: Analysed machine values.**

Machine types	M 1	M 2	M 3
Rotor pole number	11	13	13
Peak airgap flux density (T)	1.7600	1.4342	1.8806
FFT phase flux linkage (mWb), on no-load	9.6969	7.9848	9.2010
FFT induced voltage (V), on no-load	4.4656	4.3456	5.0076
Reluctance torque (Nm) at rated current	0.0022	0.0067	0.0014
PM torque (Nm), at rated current	2.3363	2.2743	2.6268
Total torque (Nm), at rated current	2.3385	2.2811	2.6281
Torque per magnet volume (kNm/m <sup>3</sup> )	0.1963	0.1387	0.1670
Torque ripple (%), at rated current	10.7804	16.8509	10.4775
Total harmonic distortion (%) on no-load	5.3677	2.6013	1.9363
Magnet eddy current loss at 15A	0.0759	0.0928	0.0440

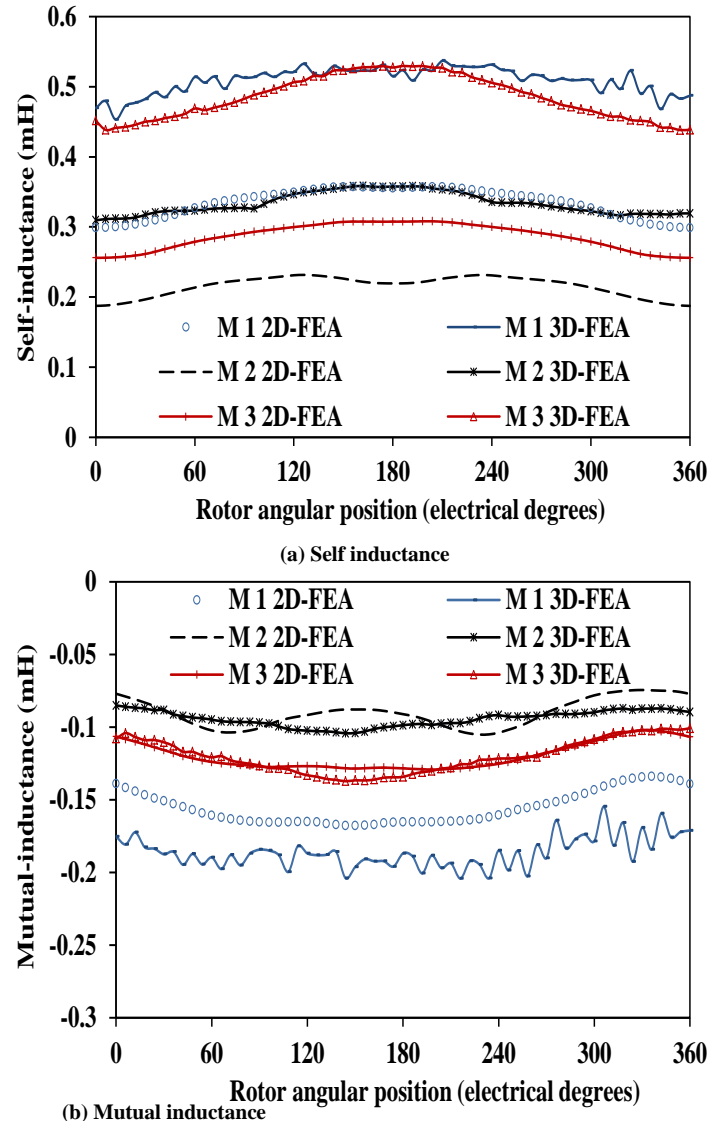
**Table 2: 2D-FEA and 3D-FEA comparisons**

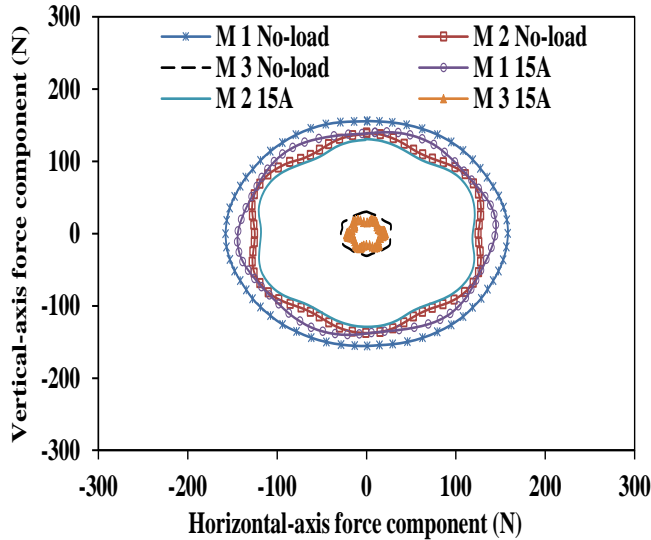
Type of Machine	M 1	M 2	M 3	M 1	M 2	M 3
Finite Element Analysis	2D FEA			3D FEA		
Peak self-inductance (mH)	0.3571	0.2316	0.3080	0.5370	0.3584	0.5296
Average self-inductance (mH), $L_{AA}$	0.3340	0.2153	0.2862	0.5087	0.3335	0.4848
Peak mutual-inductance (mH)	-0.1340	-0.0745	-0.1021	-0.1547	-0.0851	-0.1008
Average mutual-inductance (mH), $M_{AB}$	-0.1557	-0.0904	-0.1199	-0.1862	-0.0943	-0.1199
Absolute ratio of $M_{AB}$ to $L_{AA}$ (%)	46.62	41.99	41.89	36.60	28.28	24.73
Average UMF (Nm) at 15A	141.56	124.40	19.13	37.44	123.33	7.07
Torque ripple (%)	10.78	16.85	10.47	14.51	28.57	10.94

### B. Winding Inductances and Unbalanced Magnetic Force

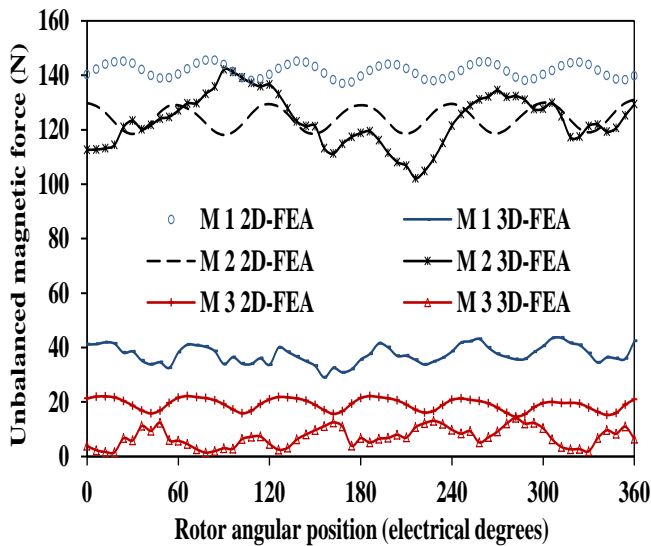
The winding inductances with respect to direct-quadrature ( $d$ - $q$ ) axes of the investigated machines are presented in Figure 9(a) and (b). It could be observed that M 1 has the largest axis inductances, and this implies that it would be more or easily vulnerable to magnetic saturation when loaded, as pointed in Thomas *et al.*, (2012), for high inductance machines. Figure 10 shows the self- and mutual-inductances of the compared machines. It is obvious that M 1 has the highest self-inductance value, which is desirable for sustaining short-circuit faults; though, M 2 has the lowest amount of mutual-inductance (machine's absolute inductance value) which is also a good quality for magnetic isolation between windings (Bianchi *et al.*, 2006), irrespective of the winding polarity. It is important to note that the recorded negative values of mutual inductances suggest that the relative polarities of the mutual windings are actually of the opposite directions. The numerical results of the compared machine types are enumerated in Table 1. More importantly, M 3 and M 2 would have competitive fault-tolerant traits, because they exhibit relatively low absolute value of mutual-inductance to self-inductance ratio, as evidenced in the 2D-FEA and 3D-FEA comparative list of Table 2. The fault-tolerance principle/concept about the least ratio of mutual-inductance to self-inductance is readily available in literature Wang *et al.*, (2012) and Tong *et al.*, (2014). This ratio indicates the level of magnetic coupling between the phase windings; thus, smaller this ratio, the better its fault-tolerance potential. Essentially, the fault-tolerant ability of any given electric machine would constantly influence the machine's overall reliability.

Figure 11 shows the outline of forces on the machines' axes and the magnitudes of unbalanced magnetic force (UMF) on the rotors of the analysed machines, under different load conditions. It is shown that the amount of UMF at rated current condition is smaller than that on no-load condition; possibly, due to the adverse effect of cogging torque which is immense

**Figure 10. Self and mutual inductances.**



(a) UMF axial components



(b) UMF versus rotor position at 15A

Figure 11. Comparison of unbalanced magnetic force.

on open-circuit situations. It is glaring that M 1 has the largest impact of this UMF defect; the least on the UMF shortcoming is M 3, which is commendable. The average UMF values of the investigated machines are also listed in Table 2. It should be noted that excessive amount of UMF in any given electric machine can lead to unwanted vibration and noise in such machine and this is similar to the effect of torque pulsation (Sung *et al.*, 2013) and (Shi *et al.*, 2020). Moreover, the noise and vibration levels in an electric machine would be a function of the adopted magnetic core materials, as established in Hou *et al.*, (2022). Furthermore, negative effect of magnetic forces could also be felt on the stator especially around its teeth; however, the magnitude of this effect can be reduced by adopting appropriate winding topology through improved winding factors (Farshadnia *et al.*, 2018). The impact of magnetic force on the stator is however not considered in this present work.

#### IV. CONCLUSION

Electromagnetic performance of three different kinds of double stator permanent magnet machine is presented. Most of the admirable machine qualities ranging from largest amount of effective air-gap flux density, low torque ripple and THD values, little UMF level to the best fault-tolerant potential is exhibited by M 3 machine type; thus, making it the most competitive candidate amongst the compared machines. However, M 1 machine topology has the best performance, in terms of the produced torque per quantity of utilized magnetic material, as well as the lowest cogging torque, in addition to good flux linkage quality and widest operating speed range. The compared machines would be suitable for direct drive applications.

#### STATEMENTS AND DECLARATIONS

No funding was received for conducting this study and the author has no conflict of interest (s) to declare.

#### AUTHOR CONTRIBUTIONS

**C. C. Awah:** Conceptualization, Methodology, Writing – original draft, review and editing.

#### REFERENCES

- Asgaria, S.; R. Yazdanpanah and M. Mirsalima. (2022).** A dual-stator machine with diametrically magnetized PM: Analytical air-gap flux calculation, efficiency optimization, and comparison with conventional dual-stator machines. *Scientia Iranica D*, 29(1): 208–216.
- Awah, C.C. (2022).** Performance comparison of double stator permanent magnet machines. *Archives of Electrical Engineering*, 71(4): 829–850.
- Baloch, N.; B. Kwon and Y. Gao. (2018).** Low-cost high-torque-density dual-stator consequent-pole permanent magnet vernier machine. *IEEE Transactions on Magnetics*, 54(11): 1–5.
- Bianchi, N.; S. Bolognani; M.D. Pre and G. Grezzani. (2006).** Design considerations for fractional-slot winding configurations of synchronous machines. *IEEE Transactions on Industry Applications*, 42(4): 997–1006.
- Cao, R.; C. Mi and Cheng, M. (2012).** Quantitative comparison of flux-switching permanent-magnet motors with interior permanent magnet motor for EV, HEV, and PHEV applications. *IEEE Transactions on Magnetics*, 48(8): 2374–2384.
- Chen, J.T. and Zhu, Z.Q. (2010).** Comparison of all-and alternate-poles-wound flux-switching PM machines having different stator and rotor pole numbers. *IEEE Transactions on Industry Applications*, 46(4): 1406–1415.
- Farshadnia, M.; M.A.M. Cheema; A. Pouramin; R. Dutta and E.J. Fletcher. (2018).** Design of optimal winding configurations for symmetrical multiphase concentrated-wound surface-mount PMSMs to achieve maximum torque density under current harmonic injection. *IEEE Transactions on Industrial Electronics*, 65(2): 1751–1761.
- Hou, P.; B. Ge; D. Tao; Y. Wang and B. Pan. (2022).** Coupling analysis of electromagnetic vibration and noise of

FeCo-based permanent-magnet synchronous motor. *Energies*, 15(11): 3888.

**Hwang, C.; C. Chang; S. Hung and C. Liu. (2014).** Design of high performance flux switching PM machines with concentrated windings. *IEEE Transactions on Magnetics*, 50(1): 1–4.

**Jo, I.; H. Lee; G. Jeong; W. Ji and C. Park. (2019).** A study on the reduction of cogging torque for the skew of a magnetic geared synchronous motor. *IEEE Transactions on Magnetics*, 55(2): 1–5.

**Kwon, J. and Kwon, B. (2018).** Investigation of dual-Stator spoke-type vernier machine for EV application. *IEEE Transactions on Magnetics*, 54(11): 1–5.

**Raza, M.; W. Zhao; T.A. Lipo and B. Kwon. (2017).** Performance comparison of dual airgap and single airgap spoke-type permanent-magnet vernier machines. *IEEE Transactions on Magnetics*, 53(6): 1–4.

**Shi, Z.; X. Sun; G. Lei; Z. Yang; Y. Guo and J. Zhu. (2020).** Analysis and optimization of radial force of permanent-magnet synchronous hub motors. *IEEE Transactions on Magnetics*, 56(2): 1–4.

**Sung, S.J.; G.H. Jang; J.W. Jang; J.Y. Song and H.J. Lee. (2013).** Vibration and noise in a HDD spindle motor arising from the axial UMF ripple. *IEEE Transactions on Magnetics*, 49(6): 2489–2494.

**Thomas, A.S.; Z.Q. Zhu and L.J. Wu. (2012).** Novel modular-rotor switched-flux permanent magnet machines. *IEEE Transactions on Industry Applications*, 48(6): 2249–2258.

**Tong, C.; F. Wu; P. Zheng; B. Yu; Y. Sui and L. Cheng. (2014).** Investigation of magnetically isolated multiphase modular permanent-magnet synchronous machinery series for wheel-driving electric vehicles. *IEEE Transactions on Magnetics*, 50(11): 1–4.

**Ullah, W.; F. Khan and S. Hussain. (2022).** A comparative study of dual stator with novel dual rotor permanent magnet flux switching generator for counter rotating wind turbine applications. *IEEE Access*, 10: 8243–8261.

**Vahaj, A.A.; A. Rahideh and T. Lubin. (2019).** General analytical magnetic model for partitioned-stator flux-reversal machines with four types of magnetization patterns. *IEEE Transactions on Magnetics*, 55(11): 1–21.

**Wang, Y. and Deng, Z. (2012).** A multi-tooth fault-tolerant flux-switching permanent-magnet machine with twisted-rotor. *IEEE Transactions on Magnetics*, 48(10): 2674–2684.

**Xie, Y.; S. He; J. Shao; B. Ye; F. Yang and L. Wang. (2022).** Design and research of a dual rotor consequent-pole vernier motor with Halbach array. *IEEE Access*, 10: 53918–53927.

**Yu, J. and Liu, C. (2020).** DC-biased operation of a double-stator hybrid flux switching permanent-magnet machine. *IEEE Transactions on Magnetics*, 56(2): 1–6.

**Yu, J.; C. Liu and H. Zhao (2019).** Design and optimization procedure of a mechanical-offset complementary-stator flux-reversal permanent-magnet machine. *IEEE Transactions on Magnetics*, 55(7): 1–7.

**Zhao, J.; Y. Wang; J. Li and H. Hu. (2022).** Comparative study on torque performance of five-phase single-stator and double-stator permanent magnet synchronous motors. *CES Transactions on Electrical Machines and Systems*, 6(1): 46–52.

**Zhao, Y.; W. Huang; W. Jiang; X. Lin and X. Wu. (2021).** Optimal design and performance analysis of dual-stator permanent magnet fault-tolerant machine. *IEEE Transactions on Magnetics*, 57(2): 1–6.